Twisted clustered pinhole collimation for improved high-energy preclinical SPECT/PET

Cosmi, V.; Kvassheim, M.; Ghosh, S.; Beekman, F.J.

DOI
10.1088/1361-6560/ad8c97

Publication date
2024

Document Version
Final published version

Published in
Physics in Medicine and Biology

Citation (APA)
Cosmi, V., Kvassheim, M., Ghosh, S., & Beekman, F. J. (2024). Twisted clustered pinhole collimation for improved high-energy preclinical SPECT/PET. *Physics in Medicine and Biology*, *69*(22), Article 225016. https://doi.org/10.1088/1361-6560/ad8c97

Important note
To cite this publication, please use the final published version (if applicable).
Please check the document version above.

Physics in Medicine & Biology

IPEM Institute of Physics and Engineering in Medicine

PAPER • OPEN ACCESS

Twisted clustered pinhole collimation for improved high-energy preclinical SPECT/PET

To cite this article: Valerio Cosmi *et al* 2024 *Phys. Med. Biol.* **69** 225016

IOP Publishing Phys. Med. Biol. 69 (2024) 225016 https://doi.org/10.1088/1361-6560/ad8c97

Physics in Medicine & Biology

IPEM Institute of Physics and Engineering in Medicine

OPEN ACCESS

RECEIVED
18 June 2024

REVISED
18 October 2024

ACCEPTED FOR PUBLICATION
29 October 2024

PUBLISHED
13 November 2024

PAPER

Twisted clustered pinhole collimation for improved high-energy preclinical SPECT/PET

Valerio Cosmi[1,*], **Monika Kvassheim**[2,3], **Satyajit Ghosh**[1], **Freek J Beekman**[1,4] and **Marlies C Goorden**[1]

[1] Department of Radiation Science and Technology, Delft University of Technology, Delft, The Netherlands
[2] Department of Physics and Computational Radiology, Division of Radiology and Nuclear Medicine, Oslo University Hospital, Oslo, Norway
[3] Faculty of Medicine, University of Oslo, Oslo, Norway
[4] Free Bee International, Gouda, The Netherlands
[*] Author to whom any correspondence should be addressed.

E-mail: v.cosmi@tudelft.nl

Keywords: preclinical SPECT, collimator, high-energy, Monte Carlo

Supplementary material for this article is available online

Abstract

Objective. Advanced pinhole collimation geometries optimized for preclinical high-energy γ imaging facilitate applications such as α and β emitter imaging, simultaneous multi-isotope PET and PET/SPECT, and positron range-free PET. These geometries replace each pinhole with a group of clustered pinholes (CPs) featuring smaller individual pinhole opening angles (POAs), enabling sub-mm resolution imaging up to ~1 MeV. Further narrowing POAs while retaining field-of-view (FOV) may enhance high-energy imaging but faces geometrical constraints. Here, we detail how the novel twisted CPs (TCPs) address this challenge. *Approach.* We compared TCP and CP collimator sensitivity at equal system resolution (SR) and SR at matched sensitivity by tuning pinhole diameters for ^{18}F (511 keV) and ^{89}Zr (909 keV). Additionally, simulated Derenzo phantoms at low activity (LA: 12 MBq ml^{-1}) and high activity (HA: 190 MBq ml^{-1}) levels, along with uniformity images, were compared to assess image resolution and uniformity. *Main results.* At equal SR, TCP increased average central FOV sensitivity by 15.6% for ^{18}F and 29.4% for ^{89}Zr compared to CP. Image resolution was comparable, except for ^{89}Zr at LA, where TCP resolved 0.80 mm diameter rods compared to 0.90 mm for CP. Image uniformity was equivalent for ^{18}F, while for ^{89}Zr TCP granted a 10.4% improvement. For collimators with matched sensitivity, TCP improved SR by 6.6% for ^{18}F and 17.7% for ^{89}Zr while also enhancing image resolution; for ^{18}F, rods distinguished were 0.65 mm (CP) and 0.60 mm (TCP) for HA, and 0.70 mm (CP and TCP) for LA. For ^{89}Zr, image resolutions were 0.75 mm (CP) and 0.65 mm (TCP) for HA, and 0.90 mm (CP) and 0.80 mm (TCP) for LA. Image uniformity with TCP decreased by 18.3% for ^{18}F but improved by 20.1% for ^{89}Zr. *Significance.* This study suggests that the TCP design has potential to improve high-energy γ imaging.

1. Introduction

The continuous development of novel radiotracers and advanced imaging techniques is imperative for addressing unmet diagnostic and therapeutic requirements (Conti and Eriksson 2016, Kuker *et al* 2017). This has notably augmented the significance of high-performance preclinical SPECT and PET, pivotal for evaluating radiotracer biodistribution and potential applications.

Recently, there has been a growing interest in radionuclides, such as α and β emitters for therapeutic applications, which were previously overlooked due to the challenges in producing high-quality images of their distributions (Conti and Eriksson, 2016). For instance, ^{124}I is a positron-emitter utilized in detecting residual thyroid tissue and/or metastases in differentiated thyroid cancer (Kuker *et al* 2017) despite its long

mean positron range (3.4 mm) and several additional decay products that include high energy γ's (603 keV and 1691 keV). Similarly, ^{76}Br, although promising in tumor imaging via PET, faces implementation challenges due to its extended mean positron range (2.5 mm) and high-energy prompt γ's (559 keV) (Lovqvist *et al* 1997, Bruehlmeier *et al* 2003, Zhou *et al* 2013), which together result in blurred images and quantification errors (Laforest and Liu 2009). Another emerging radionuclide is ^{89}Zr, which has been gaining popularity thanks to its role in immunoPET (Jauw *et al* 2016). This positron emitter (23% abundance) co-emits 909 keV prompt γ's (99%), which generate a high scatter background. Other radionuclides with promising applications for high-energy radionuclide therapy include the combined γ—β emitter ^{131}I and the γ—α emitter ^{213}Bi. Their high energy γ's, respectively 364 keV and 440 keV, are extremely difficult to image with traditional SPECT.

In recent years, advanced high-energy pinhole technology has solved many of the challenges encountered when imaging such nonstandard radionuclides. This technology is integrated into the versatile emission computed tomography (VECTor) scanner currently marketed by MILabs which has been validated for sub-mm resolution SPECT and PET imaging from 30 keV up to 1 MeV γ energies (Goorden *et al* 2013). This system's capability to explore such an exceptionally wide energy range allows to image standard SPECT radionuclides as well as accurately capture tracer distributions using high-energy γ's. This has already been applied to several non-standard radionuclides mentioned above, by utilizing annihilation γ's (511 keV) resulting from positron emitters decay, or by detecting prompt γ's co-emitted by therapeutic radionuclides (α and β emitters), as well as by positron emitting tracers. This capability enables new applications such as α and β emitter imaging and simultaneous multi-isotope PET/SPECT. Imaging of high-energy γ's from ^{131}I and ^{213}Bi achieved image resolutions of 0.75 mm and 0.60 mm respectively (de Swart *et al* 2016, van der Have *et al* 2016), while simultaneous imaging of ^{99m}Tc and ^{18}F resulted in image resolution of 0.50 mm and 0.80 mm (Goorden *et al* 2013). The image resolutions for ^{131}I, ^{99m}Tc, and ^{18}F were obtained with a collimator achieving peak sensitivities of 0.16%, 0.24%, and 0.29%, respectively. Furthermore, recent studies have explored the use of prompt γ's emitted directly from the nuclei of positron emitters, thus unaffected by positron range effects. These prompt γ's enable high-resolution positron-range free PET as well as multi-isotope PET by exploiting their energy dependence. Prompt γ imaging resulted in 0.75 mm image resolution for ^{89}Zr (909 keV prompts) and ^{124}I (603 keV prompts), while multi-isotope PET was demonstrated by simultaneously acquiring ^{18}F and ^{124}I images, achieving an image resolution of 0.75 mm (Beekman *et al* 2021).

The multi-pinhole system's ability to explore a wide energy range is supported by its advanced pinhole collimation geometry, which preserves resolution at higher energies. This is accomplished by replacing traditional pinholes with a group of clustered pinholes (CP), with each cluster designed to sample the same field-of-view (FOV) of a traditional pinhole while featuring narrower individual pinhole opening angles (POAs) (Goorden and Beekman 2010, Beekman 2011). This approach addresses limitations encountered with conventional multi-pinhole collimators which suffer from pinhole edge penetration by high-energy γ's, resulting in reduced image resolution. Narrowing the POA alleviates this issue by increasing the path length that γ's travel through the pinhole edge material, making the edge a more effective barrier and reducing the likelihood of γ's penetrating it.

Further improving performance remains compelling and may demand even narrower POAs. In this work, we demonstrate that fitting such narrow POAs in a cluster comes with geometrical challenges as individual pinholes would begin to overlap. To enable clusters with narrower POAs, one can employ a 'super cluster' geometry (Beekman 2022, Nguyen *et al* 2022) or twist the pinholes around the cluster's central axis. The latter solution, denoted by twisted CPs (TCPs), is proposed and characterized in this study. The aim of this paper is to investigate the potential of TCP imaging with extremely narrow POAs and compare its performance to previous CP technology. For this purpose, we designed a TPC collimator and conducted a Monte Carlo (MC) simulation study where the sensitivity, image resolution, and uniformity of CP and TCP collimators with equal FOV were assessed by full system simulations of appropriately designed phantoms. This methodology was applied to low (12 MBq ml^{-1}) and high (190 MBq ml^{-1}) activity levels of ^{18}F and ^{89}Zr, two important tracers characterized by high-energy γ emissions of 511 keV and 909 keV respectively.

2. Materials and methods

2.1. Geometry of imaging system and collimators

In this simulation study, we compared the performance of a conventional CP collimator with a novel TCP collimator. Both collimators were assumed to be installed in the VECTor imaging system (van der Have *et al* 2009) equipped with three PMT-based large-area monolithic NaI(Tl) scintillation detectors, measuring $590 \times 470 \times 9.5$ mm^3 each, arranged in a triangular setup. Collimators compatible with the imaging system feature focusing pinhole geometries, meaning that all pinholes focus on a common volume, the central FOV

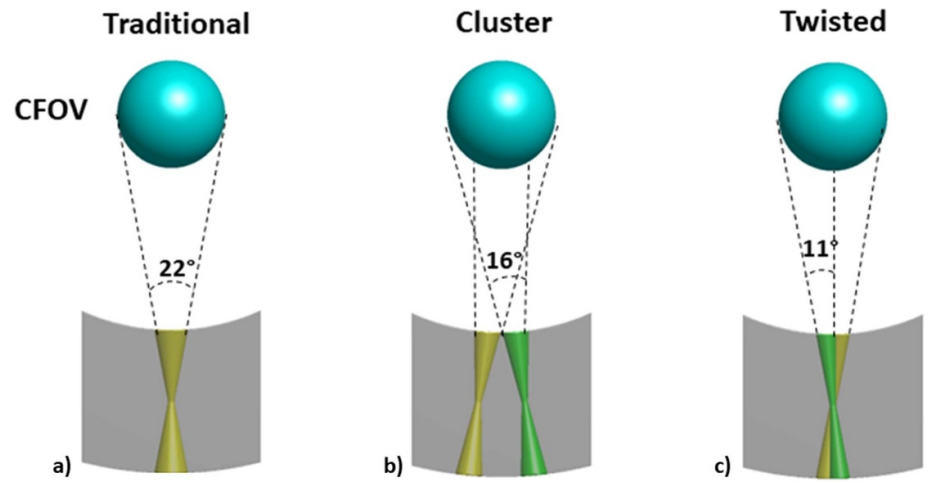

Figure 1. Illustration of various pinhole configurations. Images (a)–(c) display 2D views of traditional, clustered, and twisted clustered pinholes, respectively. Clustered and twisted cluster geometries retain the same CFOV as traditional pinholes while reducing the POA. Note that while POAs in this illustration are realistic for the collimator considered in this work, collimator thickness is reduced for improved visualization clarity.

(CFOV). Consequently, complete data acquisition for objects or organs that fit within the CFOV does not require any bed translation, while for larger objects up to whole body animal scans bed translation is done to ensure adequate sampling. Subsequently, images are reconstructed by using projection data from all the different bed positions simultaneously (Vastenhouw and Beekman 2007).

2.1.1. CP collimator design

The CP collimator, based on the design specified in a prior study (Goorden and Beekman 2010), is composed of a tungsten alloy comprising 97.0% tungsten, 1.5% nickel, and 1.5% iron. It is characterized by a cylindrical geometry with inner and outer radii measuring 24 mm and 67 mm respectively. The collimator's wall thickness is optimized for stopping 511 keV γ's and ensures that for 909 keV γ's, the probability of passing through without interaction is 0.2% for perpendicular incidence. This probability decreases for γ's that enter at non-perpendicular angles, as they traverse a greater material thickness. Furthermore, the good performance of this wall thickness for 909 keV γ's has been experimentally demonstrated (Beekman *et al* 2021).

The pinhole centers are situated at a radius of 32 mm, placed asymmetrically within the collimator wall. This configuration facilitates substantial pinhole magnification factors while utilizing the thick collimator walls that are required for high-energy γ imaging. A high pinhole magnification factor is key to high-resolution imaging since it compensates for the limited detector intrinsic resolution ($\sim$3.5 mm in this context). The CPs of 0.7 mm diameter each are grouped into 48-2 $\times$ 2 clusters, with 162 of the 192 pinholes being used for image reconstruction. Each cluster sees the ellipsoidal CFOV with principal axes of $12 \times 12 \times 9$ mm^3. These clusters are distributed across four rings, with pinholes in the outer rings exhibiting an opening angle of 16°, whereas those in the inner rings feature an opening angle of 18°. These angles ensure optimal detector coverage, resulting in a moderate projection overlap (multiplexing) of 16% at the detector's surface, which grants a reasonable fit of the elliptical pinhole projections onto the flat detector's surface (Mok *et al* 2009). Compared to conventional pinhole collimators (figure 1(a)) that can be accommodated on the same platform for traditional SPECT energies, the CP collimator (figure 1(b)) has reduced opening angles while maintaining an equivalent CFOV (van der Have *et al* 2009).

Further reducing the POAs of the CP collimator could be a suitable solution to improve system performance. However, the current design constraints preclude such adjustments, as will be elaborated in the following section.

2.1.2. TCP collimator design

The TCP collimator we propose can be conceived as an evolution of the CP collimator, thus they share numerous characteristics. We kept consistency in parameters such as material composition, CFOV size, number of pinholes per cluster, degree of multiplexing, inner and outer radii of the collimator, and radius at which pinhole centers are placed. The only variable we altered was the placement of individual pinholes and their opening angles. This allows to perform identical imaging studies with both collimator types, while solely assessing the effect of the new TCP geometry.

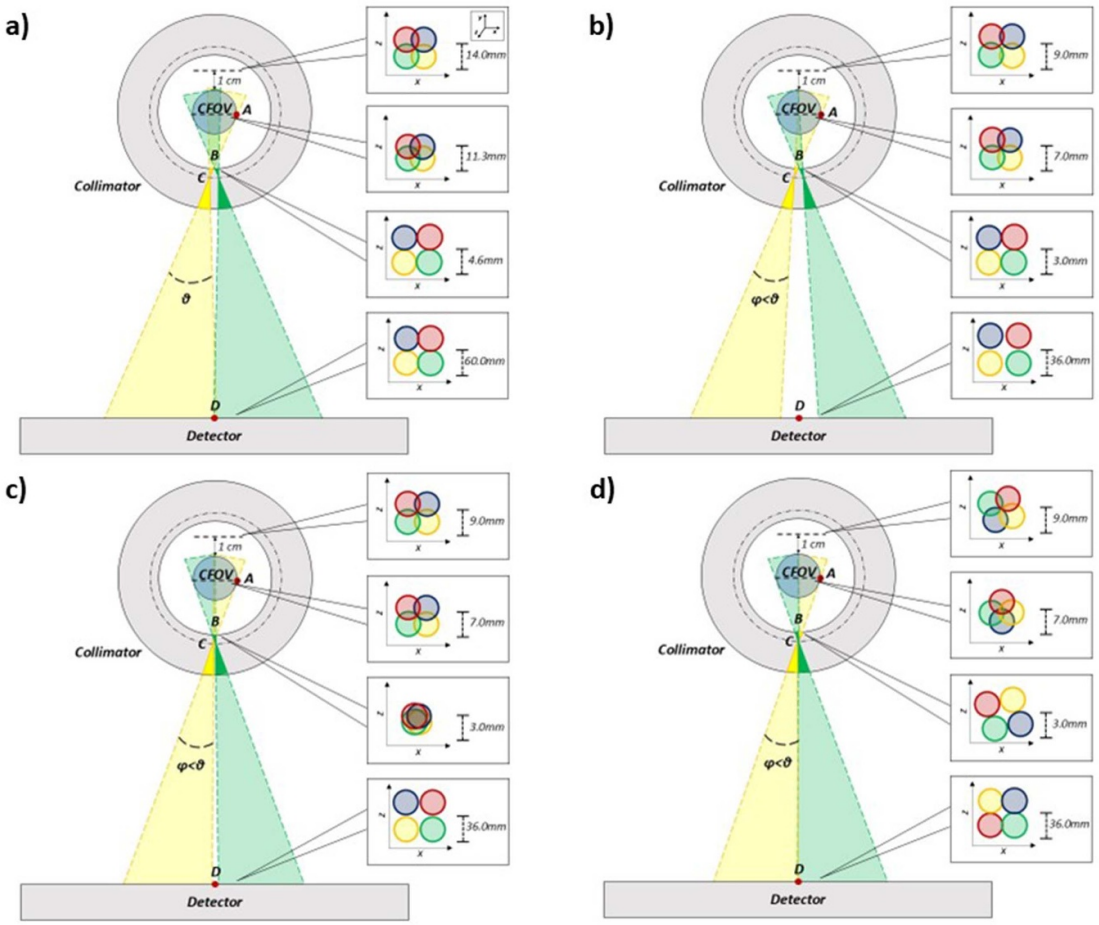

Figure 2. Schematic representation of challenges in narrowing POAs in CP technology and the solution in terms of TCP. The figure shows frontal views featuring two of four pinholes within a cluster and cross-sectional planes (*xz*-plane, with the *z*-axis pointing in the direction perpendicular to the page) showing all four pinholes. Image (a) illustrates the current CP design with POAs θ, wherein the 'green' and 'yellow' pinholes are situated in the same plane. In (b), reduced POAs ($\varphi < \theta$) result in incomplete detector surface coverage. To address this limitation while retaining CFOV sampling, pinholes are inwardly rotated in (c), causing pinhole overlap within the collimator as shown in the *xz* plane cross-section. Twisting pinholes around the cluster's central axis in (d) overcomes these limitations, as pinholes lay in different planes. The image shown in (d) closely resembles the final cluster design used for the TCP collimators. Note that for the twisted pinholes design in (d), the relative position of all four pinholes in the *xz*-plane changes.

The design concept of the TCP collimator can be visualized by describing the process for reducing POAs of CP and illustrating the constraints preventing this. For illustrative purposes, we consider each pinhole as consisting of two cones without depicting the finite hole diameter (figure 2).

In the CP collimator, individual pinholes are defined by two lines: one tangent to the desired CFOV, and a second one determining the opening angle and projection size onto the detector. Assuming a design wherein pinholes in a cluster do not overlap (figure 2(a)), the line tangent to the CFOV (point A) is required to intersect point B (where the two pinholes touch without overlapping). The second line instead should cross the first line at the pinhole center (point C) and extend to point D on the detector to guarantee complete coverage of the detector surface while avoiding projection overlap (figure 2(a)). These observations imply that, given the CFOV and the condition that individual pinholes do not overlap while utilizing the entire detector surface, the POA for a 2×2 cluster is determined (θ).

Expanding upon this concept, suppose that we reduce the POA ($\varphi < \theta$) with such a design. In figure 2(b) it is shown that simply reducing the POA while preserving the tangential line to the CFOV (line AB) would result in a gap between pinhole projections on the detector near point D. One possible approach to reduce this involves inward rotation of pinholes around point A (figure 2(c)). However, this adjustment would lead to an overlap among individual pinholes in the collimator, as they are located in the same plane (figure 2(c)). This defies the intention of CP, whose aim is to minimize collimator penetration by increasing the amount of material traversed by photons when they do not go directly through the pinhole.

The new TCP collimator adopts the strategy illustrated in figure 2(c) of moving pinholes closer to each other to reduce their opening angles. Ideally, this would be possible if the two pinholes illustrated in figure 2

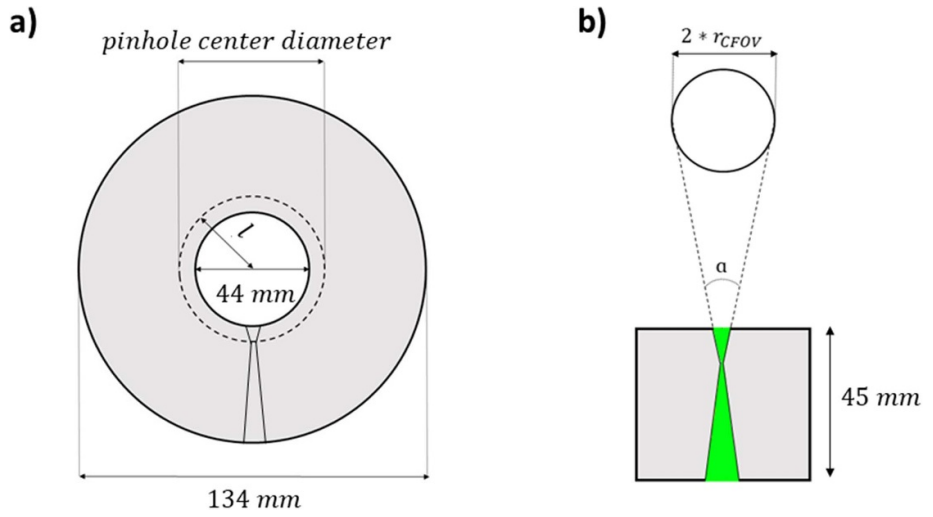

Figure 3. Schematic representation of the collimator geometry. (a) Frontal view of the collimator with collimator radii provided that are valid for both TCP and CP designs, while l represents the distance from pinhole center to collimator center. The outline of a single traditional pinhole is visible. (b) Illustration of a cross section of a traditional pinhole collimator, where r_{cfov} indicates the CFOV radius and α the opening angle of an individual pinhole.

would not be in the same plane. However, merely shifting the pinhole in the direction perpendicular to the paper would lead to overlap with other pinholes within the 2 × 2 cluster. Instead, we accomplish this by twisting individual pinholes within a cluster around the cluster's central axis, ensuring that all four pinholes reside in distinct planes (figure 2(d)). This adjustment guarantees that, as with CP, every point within the CFOV is sampled by at least one pinhole. This was additionally checked by MC simulations. Furthermore, it allows to preserve collimator material separating the pinholes while reducing their opening angles.

The TCP design is expected to be more focused compared to CP, as evident from the differing extents of pinhole cone overlap in CP (figure 2(a)) and TCP (figure 2(d)). To comprehend the implications of such difference, sensitivity over the CFOV volume, as well as over larger volumes, will be examined.

As will be discussed later, a standard design for the TCP collimator was defined. Such collimator was used as a reference for different twisted designs, where pinhole diameter and amount of cluster's twisting were varied to grant a fair comparison between TCP and CP collimators.

2.1.3. Cluster arrangement in TCP collimator

As illustrated in figure 1, the TCP collimator allows for pinholes with half the POA of a traditional pinhole, while maintaining the same CFOV. As a result, the size of the projection of the whole cluster on the detector is comparable to that of traditional pinhole projections. Therefore, during the collimator design phase it is convenient to start with a traditional pinhole collimator housing pinholes that view the desired CFOV and then later replace them with a twisted cluster. The traditional POA a corresponding to the desired CFOV is given by the following equation:

$$a = 2 \cdot \sin^{-1}\left(\frac{r_{\mathrm{CFOV}}}{l}\right). \tag{1}$$

Here r_{CFOV} is the CFOV radius, set to 6 mm (figure 3(b)) to match that of the CP collimator; l is the distance of the pinhole center to the collimator's center (figure 3(a)). This distance is calculated by combining the pinhole center radius (32 mm) and the axial shift of the ring on which the pinhole is placed.

Using an AutoCAD script, we proceeded to design a collimator with traditional pinholes. These pinholes were characterized by opening angles of 22°, calculated via (1) to grant the desired CFOV ($12 \times 12 \times 9$ mm^3). A total of 108 traditional pinholes were distributed across six rings to achieve full detector coverage. The pinholes in each ring were evenly spaced, resulting in uniform angular separation between pinholes. To evaluate detector coverage, the intersections of the extension of the pinhole cones with the detector surface were determined. Subsequently, these traditional pinholes were replaced with clusters of 2 × 2 twisted pinholes with the same FOV (figure 4).

The centers of the TCPs, the shift between clusters within the same ring, and the amount of twisting, were all fine-tuned through an iterative process. The twisting angle, indicated by the angle between the pinhole's axis and the normal to the cluster's axis, was calculated via equation A1. These parameters underwent gradual variation as we visually examined the geometric projection of the pinholes onto the

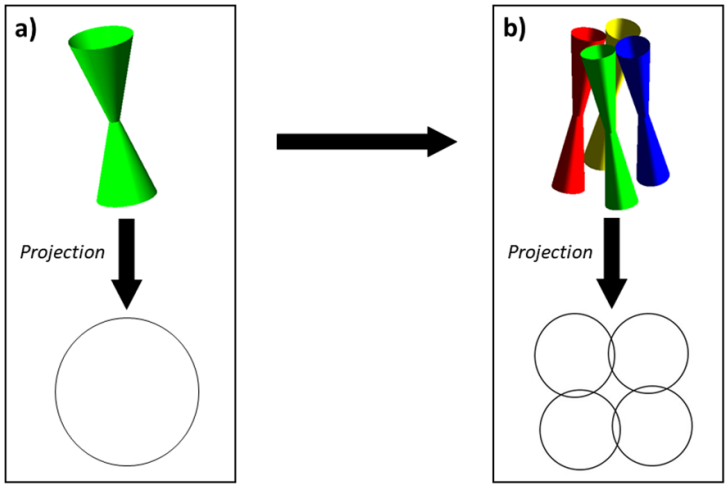

Figure 4. Visual representation of the procedure for placing the twisted clusters on the collimator's surface. For visualization purposes, symmetric pinholes with shorter lower cones than in the designed collimator are shown here. Image (a) shows a single traditional pinhole, replaced in (b) by a cluster of 2 × 2 pinholes twisted around their central axis. An iterative process defines the cluster's position and degree of twisting. Further adjustments to the amount of twisting and the placement of clusters are discussed in section 3.2.

detector and assessed the degree of multiplexing (figure 4(b)). The latter was calculated by verifying for each detector pixel center whether it was within the surface defined by a single or multiple pinhole projection cones (figures 5(c) and (d))

$$\text{Multiplexing } [\%] = \frac{\#\text{pixels within multiple cones}}{\#\text{pixels with non - zero value}}. \quad (2)$$

This allowed to determine a TCP collimator with the same amount of multiplexing as the CP collimator (∼16%).

2.2. Collimator comparison

The tradeoff between system resolution (SR) and sensitivity for the CP and TCP collimators placed in the imaging system was evaluated. To ensure a fair analysis, we compared: (1) sensitivity at equal SR, and (2) SR at equal sensitivity. Meeting these criteria required iterative small adjustments of the TCP pinhole diameter and amount of cluster's twisting, resulting in the development of four distinct TCP designs, two for each radionuclide.

A detailed explanation of the equations used to establish equivalence between CP and TCP theoretical SRs is provided in the Appendix. This equivalence was obtained by initially setting the same resolution equivalent diameter d_{re} (defined in (A5)) for both collimators. The reference d_{re} values were calculated based on CP specifications, where $d = 0.7$ mm and $a = 17°$, the mean value of the opening angles in CP (16° and 18°). This calculation was performed both for ^{18}F (511 keV) and ^{89}Zr (909 keV), with the linear attenuation coefficient of the collimator material (μ) respectively 0.228 mm^{-1} and 0.135 mm^{-1}. The d_{re} values obtained, d_{re} (511 keV) = 1.15 mm and d_{re} (909 keV) = 1.46 mm, were then used to determine the TCP pinhole diameter by inverting (A5). The TCP collimators thus characterized were denoted by 'TwistResEq' and their sensitivity was calculated as explained in section 2.3.1.

To match CP and TCP sensitivity, the TCP pinhole diameters were systematically changed in steps of 0.001 mm. The final TCP designs for both radionuclides were those resulting in an average sensitivity over the entire CFOV closest to that of the CP collimator. The TCP designs obtained through this procedure were called 'TwistSensEq', their SRs were subsequently calculated using (A2).

2.3. Simulation setup and data acquisition process

The data used for the collimator comparison were generated via MC simulations using GATE v9.0, based on Geant4 version 10.05 (Jan *et al* 2004). The simulations modeled γ photon interactions with the detector without tracking their optical transport (bulk and boundary processes). The behavior of γ and optical photons was defined utilizing GATE's standard electromagnetic list of physical processes (*emstandard*). The imaging system and the phantoms used were modelled using GATE primitives.

The simulation setup consisted of the multi-pinhole imaging system equipped with either the CP or TCP collimator. The parameters of the system's triangular detector setup and of the cylindrical collimator were

derived from the manufacturer's specifications. Accordingly, the detectors' intrinsic spatial resolution was set to 3.5 mm, while the energy resolution was 9.0% and 6.7% respectively for 511 keV and 909 keV photons. These values were implemented in our analysis as we randomized the interaction energy and position for each event using Gaussian probability distributions characterized by the standard deviation (σ) calculated from the provided resolutions.

These simulations served multiple purposes, including assessing sensitivity over the CFOV and larger volumes, as well as generating forward projections of a resolution and uniformity phantom, as described in the following subsections (The number of γ's used in each case is reported in table A1).

2.3.1. Sensitivity phantom scans

The sensitivity data were obtained through simulations involving two distinct phantoms: an ellipsoidal phantom matching the dimensions of the CFOV ($12 \times 12 \times 9$ mm^3 axes), and an elliptical tube phantom with sizes $24 \times 16 \times 50$ mm^3. Additionally, an ellipsoidal volume ($24 \times 16 \times 9$ mm^3) was selected from the center of the elliptical tube phantom. Although the second phantom lacks internal structures resembling mouse anatomy, it was named the 'whole-body mouse-sized phantom' because its shape and dimensions approximate those of an actual mouse. Consequently, the ellipsoidal volume selected from its center was referred to as the 'mouse-sized phantom thick slice'.

The two phantoms were placed at the center of the collimator and were scanned for 1 h after being uniformly filled with 2 MBq ml^{-1} of ^{18}F or ^{89}Zr. The percentage sensitivity was then calculated as the ratio between the number of detected photons per decay and the total number of emissions

$$\text{Sensitivity } [\%] = 100\% * \frac{\#\text{ detected photons per decay}}{\#\text{ emissions}}. \tag{3}$$

In sensitivity analysis, it is important to acknowledge that not all detected photons provide equal information content regarding emission position. Typically, photons undergoing scattering events within the collimator or traversing the pinhole edges offer lower-quality information compared to those passing directly through pinholes. To address this, we distinguished sensitivity contributions from photons with different interaction behavior: those passing directly through the pinholes (direct), those penetrating the pinhole edges (attenuated), and those scattering within the collimator material (scattered). This differentiation was achieved by substituting the corresponding number of detected photons in (3). To determine these fractions, we conducted two sets of simulations, varying only the linear attenuation coefficient of the collimator material. In the first set, we used the standard tungsten alloy for the collimator. These simulations were employed to determine the overall sensitivity and the scattered fraction. Scattered events were identified based on their energies. In the second set, the linear attenuation coefficient of the collimator was increased by a factor of one thousand compared to the standard tungsten alloy such that only direct photons would be detected. These simulations were used to calculate the fraction of direct photons, with the remaining photons being categorized as attenuated.

The obtained data were used to calculate the average photopeak sensitivity of ^{18}F and ^{89}Zr by applying a 20% energy acceptance window around the 511 keV and 909 keV photopeak.

2.3.2. Resolution phantom scans

Image resolution was assessed by simulating a Derenzo phantom assuming a 1 h total scan across nine bed positions. These positions were arranged in a 3×3 grid with adjacent points spaced 6 mm apart in the transaxial plane, while only one axial position was used (Vaissier *et al* 2012). Given the size of the CFOV and the phantom (a cylinder with 20 mm diameter and 8 mm length) this is a conservatively high number of bed positions. Such a decision was made to ensure adequate sampling of the object, with every part of the scan volume covered by the CFOV at least once. The phantom contained six sectors featuring cylindrical rods with diameters of 0.90 mm, 0.80 mm, 0.75 mm, 0.70 mm, 0.65 mm, and 0.60 mm. Each rod had a height of 6 mm, and the distance between their centers within each sector was twice their diameter. The rods were filled with either low or high activity concentrations, respectively 12 MBq ml^{-1} and 190 MBq ml^{-1}, of ^{18}F or ^{89}Zr. This allowed to evaluate performance at different activity levels.

2.3.3. Uniformity phantom scans

To evaluate uniformity, we designed a cylindrical phantom with 14 mm diameter and 6 mm length filled uniformly with 2 MBq ml^{-1} of either ^{18}F or ^{89}Zr. The scan sequence comprised the same nine bed positions as for the Derenzo phantom, with a total scan duration of 1 h.

2.4. Image reconstruction

Prior to reconstruction, we applied an energy acceptance window of 20% around the ^{18}F and ^{89}Zr photopeaks, centered respectively at 511 keV and 909 keV. Furthermore, a triple-energy window scatter correction method was implemented by defining two side windows adjacent to the photopeak, each having a width of 25% of the photopeak window's width (Ogawa *et al* 1991).

We generated system matrices for each collimator and radionuclide analyzed. These energy dependent matrices were calculated with a ray-tracer which considers attenuation in the collimator and detector while it ignores scatter (Goorden *et al* 2016). The system matrices for ^{18}F and ^{89}Zr were generated using the same tail cutoff (1% Goorden *et al* 2016) and differ solely due to the use of different attenuation coefficients in the ray-tracer software for the collimator and detector. Although the software and hardware were initially designed for 511 keV γ's, their effectiveness for higher energies, such as the 909 keV prompt γ's from ^{89}Zr, has been experimentally validated (Beekman *et al* 2021).

Images were reconstructed via the recently developed dual-matrix dual-voxel pixel-based similarity-regulated ordered subsets expectation maximization (SROSEM) method (Goorden *et al* 2020). This algorithm employs two voxel sizes to accelerate reconstruction, with larger voxels used to model the slowly varying PSF tails and smaller voxels for the central parts of the PSFs. We defined the central part of the PSF as the part with values down to 20% of its peak value (modelled with 0.4 mm voxels), while the tails were defined as the part with smaller values (modelled with 0.8 mm voxels). During backprojection, only the central part of the PSFs was used. This accelerated photon transported modelling was integrated with SROSEM, an accelerated ordered subset algorithm that automatically and locally adapts the number of subsets, with a maximum of 128 subsets (Vaissier *et al* 2016).

The images obtained underwent post-filtering using a series of 3D Gaussian filters with different FWHMs. For the resolution phantom, these FWHMs were the ones optimizing the contrast to noise ratio (CNR) of selected rod sectors (the inspected sectors are indicated in the corresponding image captions, and the filter values are listed in table A2). For the uniformity phantom instead, a 1.0 mm filter was applied.

2.5. Data analysis

Data from the sensitivity, resolution and uniformity phantoms were used to quantitatively evaluate the TCP and CP collimators' performance.

A contrast-noise analysis was performed on the unfiltered reconstructed images of the resolution phantom (Walker *et al* 2014). To this end, these images were resampled to a fine grid and circular regions of interest (ROI) were placed on and in between the rods. The ROIs had diameters equal to 0.9 times the rod size and were placed on 10 subsequent 0.4 mm slices of the reconstructed images. By determining the activity in each ROI, we calculated the contrast (C) in each sector (i) with the following equation:

$$C_{\text{rods},i} = \frac{\bar{h}_i - \bar{c}_i}{\bar{h}_i}. \tag{4}$$

Here $\bar{h}_i$ and $\bar{c}_i$ are respectively the mean activity in all ROIs placed on and between the rods in sector i. Furthermore, the noise in each sector (N_i) was calculated:

$$N_{\text{rods},i} = \frac{\sqrt{\sigma_{h,i}^2 + \sigma_{c,i}^2}}{\bar{h}_i + \bar{c}_i}. \tag{5}$$

Here $\sigma_{h,i}$ and $\sigma_{c,i}$ are respectively the standard deviation of the activity in ROIs on and in between rods. Using (4) and (5), the CNR was calculated and plotted against the iteration number.

Image uniformity was calculated by placing six circular ROIs with a diameter of 3.0 mm at five consecutive axial locations (evenly spaced at 0.8 mm intervals) on the reconstructed unfiltered uniformity phantom images (Walker *et al* 2014). The average value within the ROIs and the standard deviation between them, $\bar{U}$ and σ_U respectively, were measured to quantify the percentage uniformity

$$\text{Uniformity } [\%] = 100\% * \frac{\sigma_U}{\bar{U}}. \tag{6}$$

For all the configurations analyzed, the average percentage uniformity calculated over multiple simulation runs of the same setup was plotted against the number of iterations.

2.6. Convergence speed

The number of iterations required for a reconstruction algorithm to converge to the desired image is influenced by the collimator characteristics. Therefore, to grant a fair comparison between the different

collimators tested we quantified their convergence speed by calculating small detail contrast and defining an equivalent iteration number (Goorden *et al* 2020). This was done by comparing the number of iterations required by each design to achieve equal contrast for the smallest distinguishable rods filled with ^{18}F and ^{89}Zr, having diameters of 0.65 mm and 0.70 mm respectively. The contrast vs number of iterations plots of both collimators were then matched by multiplying the TCP collimator number of iterations by the constant factor that minimized the squared difference between the contrast curves.

3. Results

3.1. TCP collimator standard design

Through the design process previously described, we established a standard geometry for the TCP collimator, serving as a reference for the four different configurations examined in our analysis. These versions of the TCP collimator differ solely in terms of pinhole diameters and degree of clusters' twisting.

The TCP collimator geometry (figure 5(b)) contains 108-2 × 2 twisted clusters of 0.7 mm diameter pinholes arranged in six rings. Adjacent rings were rotated 4° relative to one other as this allowed to sample the CFOV with a larger variation in angles. In each ring, clusters were placed 8° apart. The pinhole centers of the two innermost rings were at 32.3 mm from the collimator center. For the two central and two outermost rings, this distance was 34.9 mm and 40.3 mm. After determining these distances, the pinholes placement on the inner surface was reviewed to prevent any overlap. The resulting POAs were 10.7°, 9.9° and 8.6° respectively for the two innermost, two central and two outermost rings. These opening angles appear to be narrower compared to the value initially indicated in figure 1 (11°). This is because the latter was calculated by considering a situation where the cluster was placed exactly at the central axial position of the cylindrical collimator. As clusters are positioned over several axial locations of the entire cylindrical collimator surface, their distances from the collimator's center increase and as expected from (1) their POAs diminish. Thanks to these narrower angles, the average air volume of a single TCP cluster (∼17.7 cm^3) decreased by ∼64% compared to a CP cluster (∼49.1 cm^3). Moreover, despite the increased total number of clusters (108 vs 48), the twisted design granted a ∼19% reduction in the overall air volume within the collimator due to pinholes, indicating that more collimator material is present to stop γ's.

This standard TCP geometry resulted in an amount of multiplexing comparable to the one reached by CP (figure 5(a)) with the same pinhole diameter, respectively 16.0% (figure 5(c)) and 15.7% (figure 5(d)). Details about axial sampling are provided in the supplementary material.

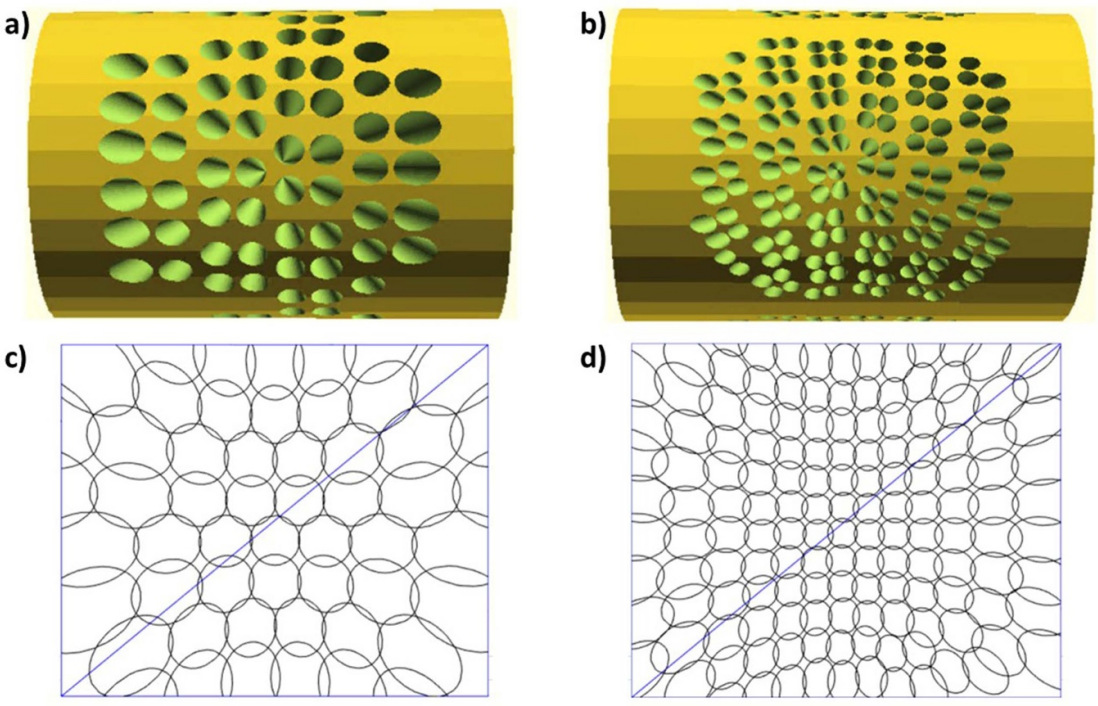

Figure 5. Visual comparison of the CP and the standard TCP collimator: a) and b) show the CP and the standard TCP collimators. The standard TCP collimator differs from those named TwistSensEq and TwistResEq solely in terms of pinhole diameter. Images c) and d) illustrate the pinhole projections on the detector surface of one of the three γ detectors for each collimator.

Table 1. Sensitivity and fraction of direct, attenuated, and scattered photons for the CP, TwistResEq and TwistSensEq collimators. Results were calculated over the CFOV, over a slice of the whole-body mouse-sized phantom, and over the whole-body mouse-sized phantom.

	^{18}F				^{89}Zr			
	CFOV (12 × 12 × 9 mm^3)							
Collimator	Sensitivity	Direct	Attenuated	Scattered	Sensitivity	Direct	Attenuated	Scattered
CP	0.32%	25.8%	65.5%	8.7%	0.17%	12.5%	83.0%	4.5%
TwistSensEq	0.32%	41.1%	50.0%	8.9%	0.17%	14.9%	80.9%	4.2%
TwistResEq	0.37%	46.0%	44.6%	9.4%	0.22%	24.2%	72.1%	3.7%
	Mouse-sized phantom thick slice (24 × 16 × 9 mm^3)							
CP	0.23%	25.1%	63.7%	11.2%	0.14%	10.3%	84.7%	5.0%
TwistSensEq	0.22%	37.7%	50.4%	11.9%	0.13%	11.7%	83.5%	4.8%
TwistResEq	0.26%	42.8%	45.9%	11.3%	0.18%	19.3%	76.3%	4.4%
	Mouse-sized phantom (24 × 16 × 50 mm^3)							
CP	0.096%	18.1%	61.4%	20.5%	0.097%	4.4%	89.0%	6.6%
TwistSensEq	0.087%	27.2%	51.9%	20.9%	0.091%	5.0%	88.0%	7.0%
TwistResEq	0.10%	31.5%	49.3%	19.2%	0.11%	8.9%	84.7%	6.4%

3.2. Collimator performance comparison

To achieve a SR equivalent to that of the CP collimator, which has a 0.7 mm pinhole diameter and an average POA of 17°, the required pinhole diameters for the TCP design were calculated using equation (A5), assuming an average POA of 9.7°. The resulting diameters were 0.896 mm for 511 keV and 1.030 mm for 909 keV γ's, representing an increase from the 0.7 mm pinhole diameter in the previously described standard TCP design.

Adjusting the standard TCP collimator diameter to these new values affected the CFOV and the multiplexing, as both parameters increased compared to the values obtained with the reference twisted design employing 0.7 mm diameter. These issues were addressed by reducing the amount of twisting (A1) until the CFOV and multiplexing returned to their original value. Additionally, for the 1.030 mm pinhole design, an overlap of two clusters on the outer ring was noticed. To prevent that, one of these clusters was rotated outward by 1° relative to its axis. The TCP designs achieving sensitivity equivalent to that of CP over the CFOV feature slightly larger pinhole diameters than the standard TCP design, with diameters of 0.788 mm and 0.725 mm, respectively for ^{18}F and ^{89}Zr. No additional adjustments were necessary for these designs since these values did not impact the CFOV and multiplexing.

The sensitivity performance of the TwistResEq and the TwistSensEq collimators compared to the CP collimator is summarized in table 1 for the different-sized sensitivity phantoms.

For the average sensitivity over the CFOV, the values achieved with the TwistResEq showed an increase of 15.6% and 29.4% for ^{18}F and ^{89}Zr respectively, compared to the CP collimator. Furthermore, results indicate that most of the photons detected within the photopeak traversed the pinhole edges (denoted by 'attenuated' in table 1), rather than passing directly though the pinhole opening. Nonetheless, TCP demonstrated a higher relative number of photons going directly through the pinhole compared to CP; while for CP only 25.8% and 12.5% of the photons passed directly through the hole for ^{18}F and ^{89}Zr respectively, these percentages increased to 46.0% and 24.2% for the TwistResEq, and to 41.1% and 14.9% for the TwistSensEq. This increased fraction of direct photons came at the expense of attenuated photons, as the relative amount of pinhole scatter remained similar across different designs.

Evaluating the sensitivity over the larger mouse-sized phantom, the TwistResEq still granted noticeable improvement compared to the CP collimator. Specifically, within the selected confined region of this phantom, sensitivities increased by 13.0% for ^{18}F and by 28.6% for ^{89}Zr. When considering the entire mouse-sized phantom volume instead, smaller improvement of 4.2% and 13.4% were observed. On the other hand, the TwistSensEq sensitivity results indicated a slight performance degradation compared to CP. Over the selected volume region, this sensitivity reduction was of 4.3% and 7.1% for ^{18}F and ^{89}Zr respectively, whereas over the entire phantom volume it was of 9.4% and 6.2%. The trends observed for direct, attenuated, and scattered fractions of photons exhibited behaviors consistent with those described for the CFOV. The fractions of direct photons observed over a region of the whole-body phantom with the CP collimator were 25.1% and 10.3% respectively for ^{18}F and ^{89}Zr. These values increased to 42.8% and 19.3% with the TwistResEq, and to 37.7% and 11.7% with the TwistSensEq. Similarly, for the whole-body phantom

Table 2. System resolution, pinhole diameter and effective diameter for the CP, TwistResEq and TwistSensEq collimators.

	^{18}F			^{89}Zr		
Collimator	SR	d	d_{re}	SR	d	d_{re}
CP	1.52 mm	0.70 mm	1.15 mm	1.86 mm	0.70 mm	1.46 mm
TwistSensEq	1.42 mm	0.79 mm	1.05 mm	1.53 mm	0.73 mm	1.16 mm
TwistResEq	1.52 mm	0.90 mm	1.15 mm	1.86 mm	1.03 mm	1.46 mm

CP achieved a relative number of direct photons of 18.1% for ^{18}F and 4.4% for ^{89}Zr, which improved to 31.5% and 8.9% with the TwistResEq, and to 27.2% and 5.0% with the TwistSensEq.

The SR, pinhole diameter (d) and effective diameter (d_{re}) of the collimators tested are provided in table 2.

The TwistSensEq designs improved SR by 6.6% and 17.7% for ^{18}F and ^{89}Zr, respectively, in comparison to the other analyzed collimators.

3.3. Equivalent iteration number

Contrast vs. iteration number curves for 0.65 mm (^{18}F) and 0.70 mm (^{89}Zr) rods in the Derenzo phantom were used to establish equivalent iteration numbers for different collimator types.

Our findings revealed that collimator designs with matched SRs converged at comparable speed. Therefore, images obtained with the TwistResEq and the CP collimators were compared at equal iteration number both for ^{18}F and ^{89}Zr. On the other hand, when matching sensitivity, images obtained by the TCP collimator converged faster than those obtained with CP for both radionuclides analyzed. It was determined that 1 CP iteration is equivalent to 1.62 TwistSensEq iterations for ^{18}F (figure A1), while for ^{89}Zr 1 CP iteration corresponds to 3.00 TwistSensEq iterations (figure A1).

3.4. Resolution phantom simulations

Reconstructed images of the resolution phantom filled with 12 MBq ml^{-1} or 190 MBq ml^{-1} of ^{18}F are shown in figure 6 for different numbers of (equivalent) iterations.

A visual inspection of the results achieved with the TwistResEq and CP collimators indicates comparable performance, as for both configurations the smallest distinguishable rods have 0.70 mm diameter at low activity and 0.65 mm diameter at high activity. Images reconstructed with the TwistSensEq demonstrate equivalent performance to those obtained with other collimators at low activity levels. However, at higher activity levels, the TwistSensEq shows moderate improvement, with rods of 0.60 mm becoming more easily identifiable at 60 and 190 iterations. This can be seen in figure 8(a), which displays profiles of the smallest distinguishable rod sectors extracted from the resolution phantom images at the highest shown iteration number: 190 for CP and TwistResEq, and 117 for TwistSensEq.

Figure 7 shows the images of the resolution phantom filled with 12 MBq ml^{-1} or 190 MBq ml^{-1} of ^{89}Zr for different numbers of (equivalent) iterations.

At low activity, the TwistResEq shows superior performance compared to the CP design, as the former could resolve rods of 0.80 mm diameter, while the latter could discern rods of 0.90 mm. Performance of these two collimators is comparable at high activity, with the 0.70 mm rods section being the smallest distinguishable for both collimators. Upon evaluation of images reconstructed with the TwistSensEq, an overall improvement in performance relative to the CP and TwistResEq collimators can be noticed. The TwistSensEq design could distinguish rods of 0.80 mm and 0.60 mm diameter respectively at low and high activity (figure 8(b)).

3.5. Contrast and CNR analysis results

In addition to the visual comparison, a contrast-noise analysis was performed on the reconstructed resolution phantom images with results shown in figure 9, tables A3 and A4.

Figure 9 shows the average (over all visible rod sectors) CNR plotted against the equivalent number of iterations for all collimators, both for ^{18}F and ^{89}Zr.

Overall, the TwistSensEq collimator granted a noticeable CNR improvement over the CP collimator for both ^{18}F and ^{89}Zr. On the other hand, the TwistResEq has shown only a moderate (negligible for ^{18}F) performance increase. Results per rod sector are provided in tables A3 and A4 in the appendix.

3.6. Image uniformity

Reconstructed images of the uniformity phantom are shown in figure 10

These images were used to calculate the percentage image uniformity following the methodology described in the data analysis section. Results of this calculation were plotted against the equivalent number of iterations as illustrated in figure 11.

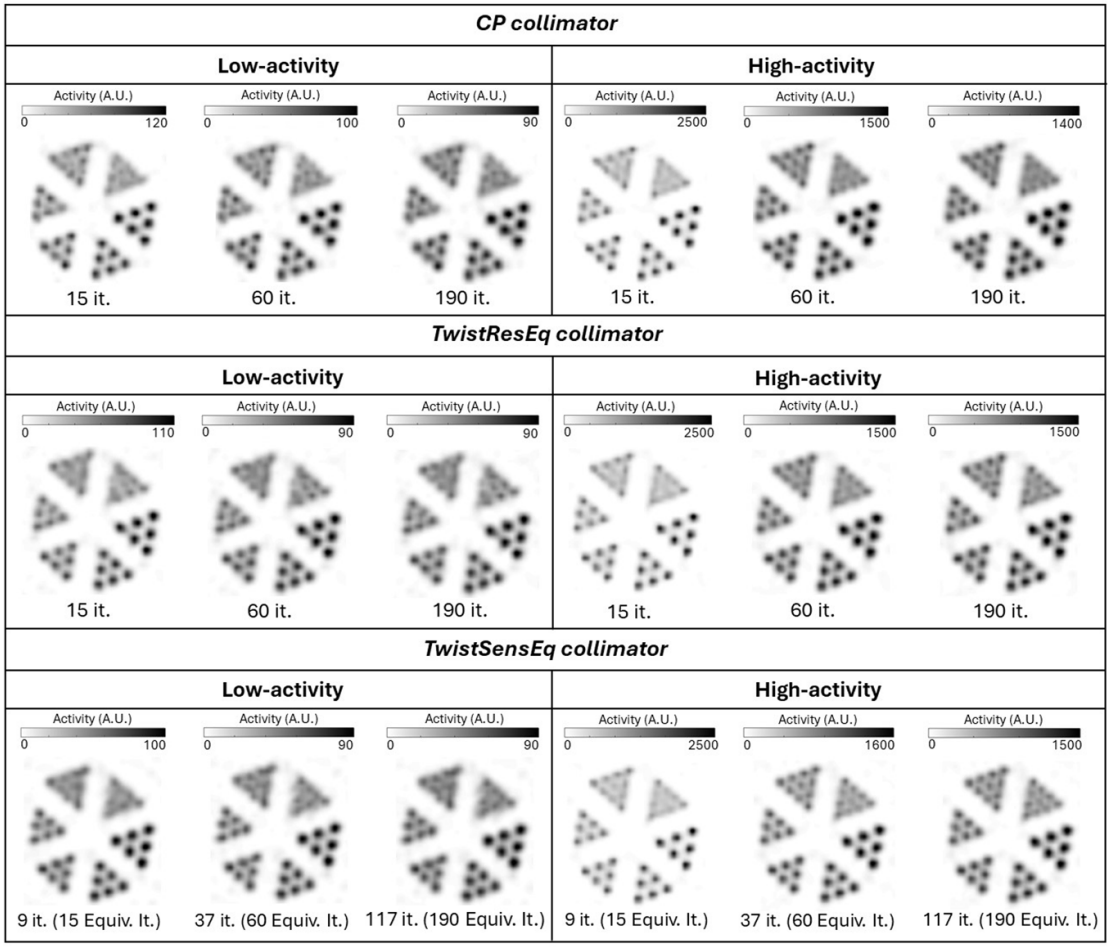

Figure 6. Resolution phantom images obtained with the CP and TCP collimators for ^{18}F. Rods with diameters of 0.90 mm, 0.80 mm, 0.75 mm, 0.70 mm, 0.65 mm, and 0.60 mm were filled with low (12 MBq ml^{-1}) or high (190 MBq ml^{-1}) activity. Based on the convergence speed analysis, images were compared at the same iteration number for collimators with matching system resolution, and at equivalent iteration numbers (Equiv. it.) for collimators with matching sensitivity. Images were post-filtered with the 3D Gaussian filters that optimized the CNR for 0.70 mm and 0.65 mm rods for both low and high activity results. The images shown were obtained by summing ten consecutive slices at the center of the phantom, resulting in a final image slice thickness of 4 mm.

For ^{18}F, the TwistResEq and the CP collimator achieved similar results, while the TwistSensEq shows an 18.3% performance deficit compared to them.

For ^{89}Zr, both twisted collimators converged to a more uniform result compared to the CP design, with an improvement of 10.4% for TwistResEq and of 20.1% for TwistSensEq.

4. Discussion

We presented the findings of a MC simulation study in which we investigated the implementation of narrower POA cones in a CP collimator with the aim to reduce pinhole edge penetration, a factor that degrades image resolution of multi-pinhole imaging systems for high-energy radionuclides. To this end, we introduced a novel pinhole arrangement for the CP collimator, wherein individual pinholes were twisted around their cluster central axis. This new design allows to reduce POAs compared to the current CP design while maintaining the same CFOV. Comparative assessments of sensitivity, image resolution and uniformity between the TCP and CP collimators were conducted for high-energy γ imaging of ^{18}F and ^{89}Zr. Results are presented in figures 6–11 and tables 1 and 2.

The analysis of average sensitivity results over the CFOV showed that the TCP collimator achieved sensitivities of 0.37% and 0.22% respectively for ^{18}F and ^{89}Zr. These values indicate improvements of 15.6% and 29.4% over those attainable with the CP collimator at the same SR. For larger volumes, sensitivity at equal SR is still better for TCP compared to CP, but improvements are smaller. These results demonstrate that TCP designs are more focused towards the CFOV and thus have the largest benefit for focused organ or tumor imaging. Nevertheless, it should be stressed that sensitivity alone does not determine image quality.

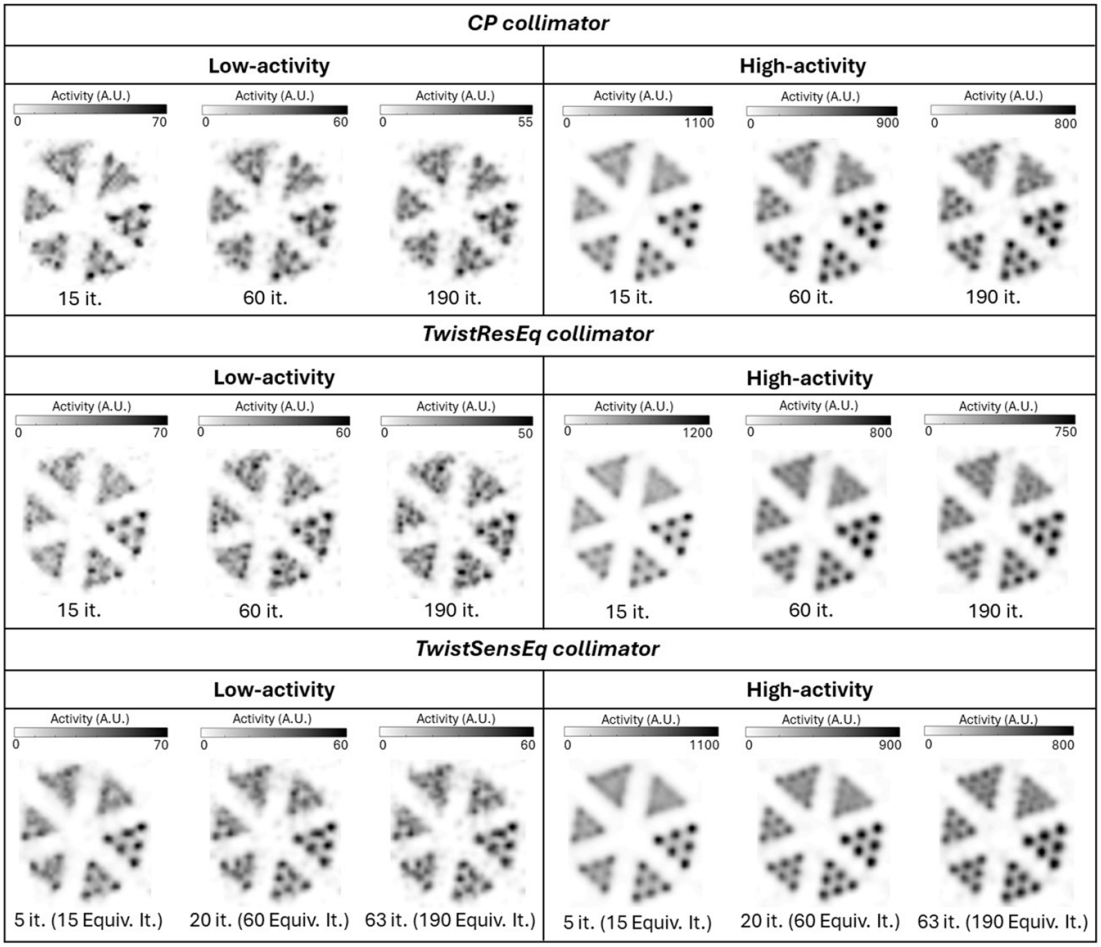

Figure 7. Resolution phantom images obtained with the CP and TCP collimators for ^{89}Zr. The rod diameters and activity levels are identical to those described in the caption of figure 6. Based on the convergence speed analysis, images were compared at the same iteration number for collimators with matching system resolution, and at equivalent iteration (Equiv. it.) numbers for collimators with matching sensitivity. Images were post-filtered with the 3D Gaussian filters that optimized the CNR for 0.75 mm and 0.70 mm rods for low and high activity results. The images shown were obtained by summing ten consecutive slices at the center of the phantom, resulting in a final image slice thickness of 4 mm.

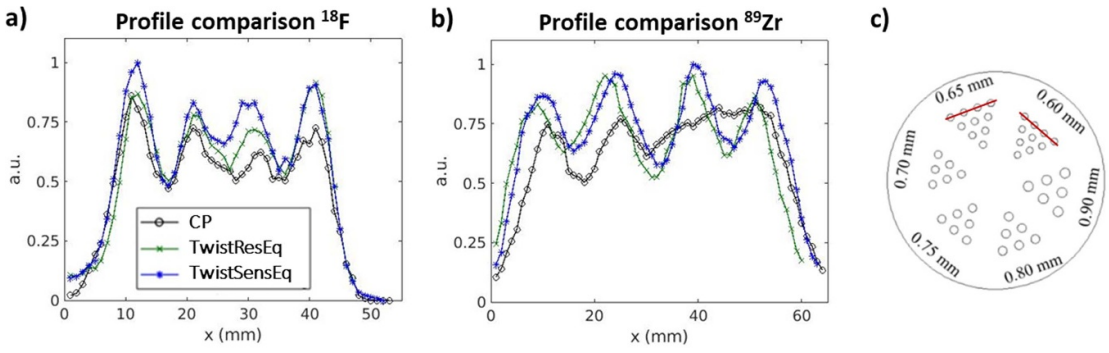

Figure 8. Profiles obtained from resolution phantom images with HA levels of ^{18}F and ^{89}Zr. The analysis was conducted on images from figures 6 and 7 with the highest number of iterations: 190 for CP and TwistResEq, and 117 for TwistSensEq for ^{18}F reconstructions; 190 for CP and TwistResEq, and 63 for TwistSensEq for ^{89}Zr reconstructions. Locations of the profiles are indicated by red lines in (c) and correspond to the 0.60 mm and 0.65 mm rod sector for ^{18}F and ^{89}Zr respectively.

Rather, it is the combination of sensitivity and the information content per detected photon that regulates the attainable level of image detail. In this context, the TwistResEq and TwistSensEq collimators significantly increase the fraction of direct photons reaching the detector compared to the CP collimator across all analyzed phantoms. Specifically, for the TwistResEq this fraction increased by 78.3% and 93.6% for ^{18}F and ^{89}Zr at the CFOV, by 70.7% and 87.4% when analyzing a portion of the whole-body phantom, and by 74.0%

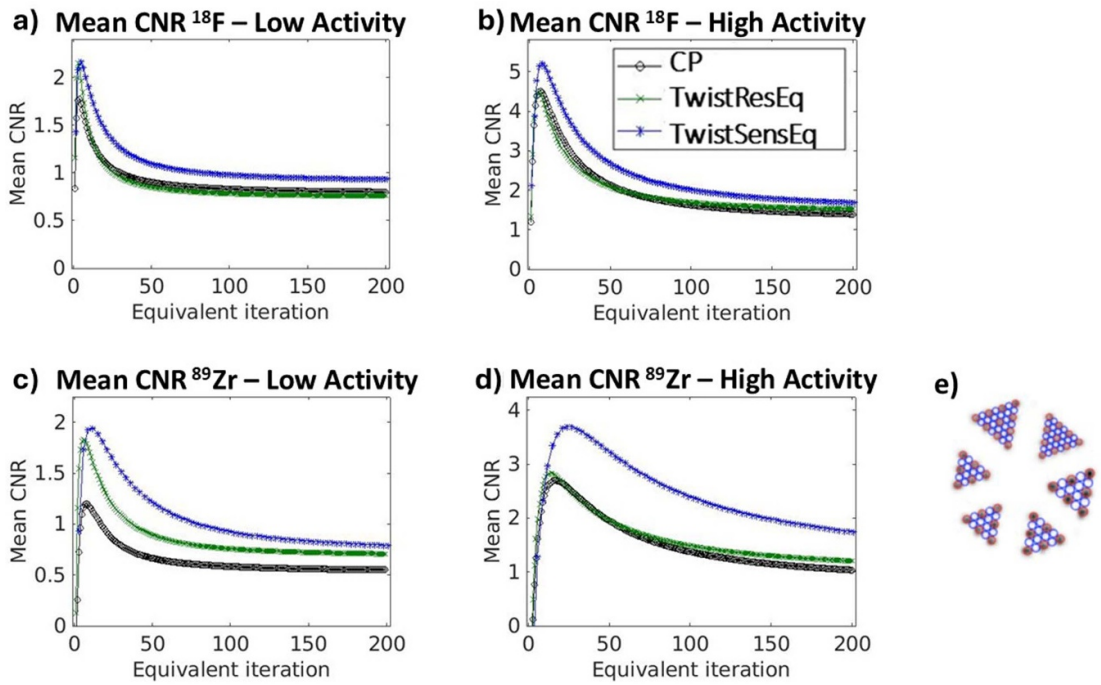

Figure 9. Mean CNRs of all tested collimators averaged over visible rod sectors and selected hot/cold regions. The CNRs are plotted against the number of equivalent iterations. Images show the results obtained for rods filled with low (12 MBq ml^{-1}) and high (190 MBq ml^{-1}) activity of ^{18}F (a), (b) and ^{89}Zr (c), (d). Image (e) shows an example of the ROIs selection applied to the reconstructed resolution phantom images. Red circles are placed on the rods, while blue circles are positioned in between rods.

and 102.3% when considering the entire volume of the mouse-sized phantom (table 1). This may be advantageous since these direct photons are expected to carry more precise information about the emission locations compared to photons that penetrated the pinhole edges. However, quantitively estimating the impact of such improvement on image quality is complex. Regarding the sensitivity differences observed between the ^{18}F and ^{89}Zr simulations, these are influenced by two opposing factors. On one hand, the detector has lower sensitivity for ^{89}Zr high energy γ's. On the other hand, these γ's emitted by ^{89}Zr are more likely to penetrate the collimator material. This effect is amplified in larger phantoms, where regions outside the CFOV are covered by fewer clusters, or sometimes not covered at all. As a result, the sensitivity for ^{89}Zr in larger phantoms becomes closer to that of ^{18}F.

Results of the SR analysis indicate a moderate advantage for the TCP over the CP collimator (table 2). Matching the CP SR with the TwistResEq design yielded visually equal images for both activity levels of ^{18}F and ^{89}Zr except for the images obtained for the low activity ^{89}Zr distribution, where slightly better results were observed for the TwistResEq collimator, resolving 0.80 mm diameter rods compared to the 0.90 mm of CP (figure 7). Such improvement may be attributed to the increased fraction of direct photons detected by the twisted design (table 1). The TwistSensEq design instead outperformed the CP for both radionuclides analyzed, improving SR by 6.6% and 17.7% for ^{18}F and ^{89}Zr respectively. Regarding image resolution, for ^{18}F both collimators performed equally at low activity levels (figure 6) resolving 0.70 mm diameter rods, but at high activity the TwistSensEq distinguished 0.60 mm diameter rods compared to the 0.65 mm ones solved by the CP. For ^{89}Zr, the TwistSensEq discerned 0.80 mm and 0.65 mm rods at low and high activity levels, respectively, compared to the CP's 0.90 mm and 0.75 mm rods (figure 7). Resolving sectors containing small rods (<0.80 mm) filled with low activity of ^{89}Zr proved to be challenging for every collimator design tested. Overall, the TwistSensEq granted the best results for both radionuclides. Additionally, although a specific analysis of partial volume effect was not included in this work, we partially correct for it in the reconstruction through PSF modeling, and its influence can be observed in the reconstructed resolution phantom images (figures 6 and 7).

The CNR analysis indicated an increase in performance with the twisted designs (figure 9). For ^{18}F, CNR results obtained with the TwistSensEq design surpassed those of the CP and TwistResEq collimators at both low and high activity levels (figures 9(a), (b), tables A3 and A4). Such an increase aligns with the expectations, considering the slightly improved SR achieved by the TwistSensEq design (table 2). For ^{89}Zr (figures 9(c) and (d)), the twisted designs granted moderately better CNR performance than CP across both activity levels, with the TwistSensEq exhibiting the highest CNR values among the three collimators (tables A3 and A4).

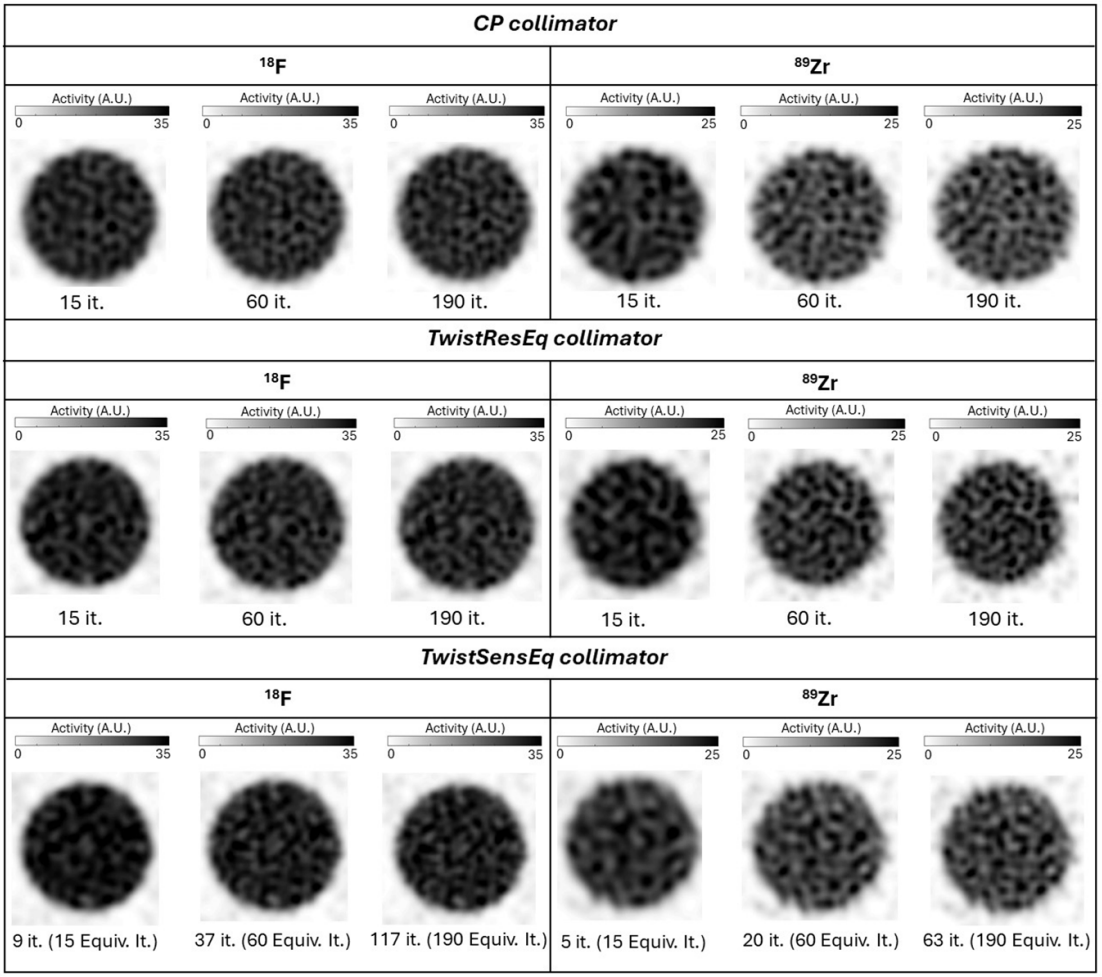

Figure 10. Images of the uniform phantom reconstructed using CP and TCP collimators. Based on the convergence speed analysis, images were compared at the same iteration number for collimators with matching system resolution, and at equivalent iteration numbers (Equiv. it.) for collimators with matching sensitivity. Images shown were post-filtered with a 3D Gaussian filter having a FWHM of 1 mm. The images shown were obtained by summing ten consecutive slices at the center of the phantom, resulting in a final image slice thickness of 4 mm.

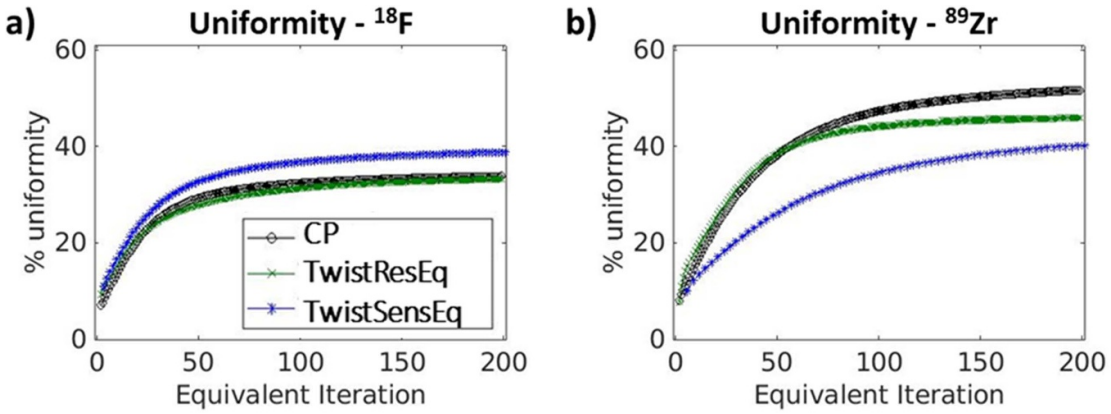

Figure 11. Average percentage uniformity of the collimators simulated for ^{18}F (left) and ^{89}Zr (right). Results were plotted against the equivalent number of iterations.

In the assessment of image uniformity, twisted collimators obtained slightly more uniform images for both radionuclides. Although visually inspecting the reconstructed uniform phantom images (figure 10) may not readily convey these differences, they become evident upon examination of the uniformity trend plots (figure 11). In this case the TwistResEq granted the best results, with comparable performance for ^{18}F and a

10.4% improvement for ^{89}Zr. For the TwistSensEq instead, performance resulted to be degraded of 18.3% for ^{18}F, while an improvement of 20.1% was observed for ^{89}Zr.

It is important to note that the imaging system simulated uses a 9.5 mm thick scintillator, which is not optimal for detecting the high-energy 511 keV or 909 keV prompt γ's. Previous research (Cosmi *et al* 2024) indicated that increasing the scintillator's thickness to 19 mm or 40 mm roughly doubles or quadruples detection efficiency for 511 keV γ's (from ∼12% to ∼27% or ∼53%). A similar improvement can be expected for 909 keV γ's. However, since our goal was to compare collimator performance, we used the most commonly available detector configuration, which typically employs 9.5 mm thick crystals, although 19 mm crystal thickness is also available.

In this work, we analyzed a 2 × 2 cluster, though larger clusters (e.g. 3 × 3) are theoretically possible. While these could provide more pinholes with narrower angles, they would increase system complexity. The higher number of pinhole projections would complicate calibration, and manufacturing may become more challenging due to the higher precision required for smaller pinholes. Therefore, in this work we focused on a 2 × 2 cluster, with the potential for exploring larger clusters in the future.

5. Conclusion

We introduced an improved arrangement of pinholes for the CP collimator, aimed at further mitigating the adverse effects of pinhole penetration in high-energy SPECT imaging. To this end, we presented a collimator characterized by clusters of 2 × 2 pinholes twisted around the cluster's axis, termed TCP collimator. Employing this novel collimator on a multi-pinhole preclinical scanner, we compared its performance to that of traditional CP collimators. Simulations indicate that the TCP collimator offers improved sensitivity and SR compared to the CP collimator. Image uniformity resulted to be equivalent for ^{18}F, while for ^{89}Zr TCP granted a noticeable improvement.

Data availability statement

All data that support the findings of this study are included within the article (and any supplementary information files).

Acknowledgment

This work was financed by the research grant QUARAT: Quantitative Universal Radiotracer Tomography (TTW16885) which is financed in part by the Dutch Research Council (NWO).

Conflict of interest

The authors declare no conflicts of interest to disclose.

Appendix

Twisting angle

$$\text{Twisting angle} = \frac{\delta * \gamma}{\theta}. \tag{A1}$$

Here δ is the angle between the CFOV axis and the three-dimensional distance between the pinhole and the CFOV center; γ is an arbitrarily defined value expressed in degrees determining the rotation intensity, and θ is the angle between the CFOV axis and the pinhole center radius.

Matching SR

The SR was calculated as:

$$\text{SR} = \sqrt{\left(\frac{R_i}{M}\right)^2 + R_{\text{coll}}^2}. \tag{A2}$$

Here R_i indicates the detector's intrinsic spatial resolution, R_{coll} the collimator's geometric resolution, and M the magnification factor, defined as:

$$M = \frac{b}{l}. \tag{A3}$$

Here b is the average distance from the detector to the pinhole centers (∼178 mm), and l the average distance from the object to the pinhole centers (∼34 mm). Its value was calculated to be ∼5.2 for all the designs analyzed. The term R_{coll} is dependent on the collimator's geometry according to the following equation:

$$R_{coll} = d_{re}\left(\frac{b+l}{b}\right) \tag{A4}$$

where d_{re} is the resolution effective diameter. The parameter d_{re} can be calculated by (Accorsi and Metzler 2004, 2005):

$$d_{re} = d + \ln(2)\,\frac{\tan\left(\frac{a}{2}\right)}{\mu}. \tag{A5}$$

Here d is the pinhole diameter and μ is the linear attenuation coefficient of the collimator material (Bom *et al* 2011). Since the collimators tested feature multiple POAs depending on their distance from the collimator's center, a used in the SR calculation was assumed to be their average.

Convergence speed

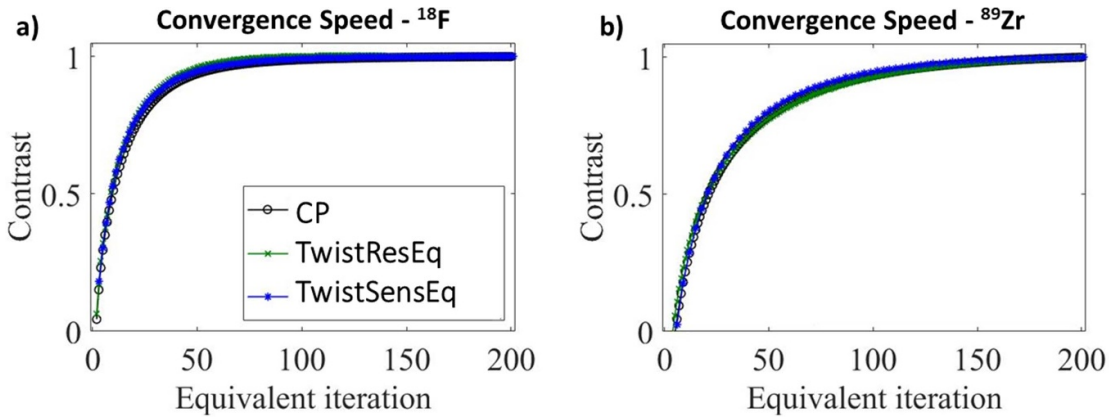

Figure A1. Comparison of convergence speed of CP and TCP collimators. Contrast of both designs was plotted against the number of equivalent iterations. Rods of 0.65 mm and 0.70 mm diameter were considered respectively for ^{18}F (a) and ^{89}Zr (b). The equivalence factor indicates the relation between CP and TCP number of iterations. Collimator designs with equivalent system resolution converged at comparable speed, therefore no equivalence factor was required. For TwistSensEq instead, it was calculated that 1 CP iteration equates to 1.62 TwistSensEq iterations for ^{18}F (a), while for ^{89}Zr 1 CP iteration corresponds to 3.00 TwistSensEq iterations (b).

Simulation data

Table A1. Number of photons emitted from the phantoms used in our simulations.

	^{18}F	^{89}Zr
Phantom	Emitted photons	Emitted photons
Sensitivity CFOV	$9.8^{*}10^{9}$	$7.0^{*}10^{9}$
Sensitivity Mouse	$2.2^{*}10^{11}$	$1.6^{*}10^{11}$
Resolution LA	$3.1^{*}10^{12}$	$3.3^{*}10^{12}$
Resolution HA	$4.9^{*}10^{13}$	$5.2^{*}10^{13}$
Uniformity	$1.3^{*}10^{10}$	$9.5^{*}10^{9}$

Gaussian filtering

Table A2. FWHMs in mm used for the 3D Gaussian post-filtering applied to the reconstructed images in figures 7 and 8.

	^{18}F			^{89}Zr		
Collimator/Activity	15 it.	60 it.	190 it.	15 it.	60 it.	190 it.
CP—LA	0.60 mm	0.70 mm	0.75 mm	0.15 mm	0.60 mm	0.65 mm
CP—HA	0.45 mm	0.70 mm	0.75 mm	0.15 mm	0.55 mm	0.65 mm
TwistResEq—LA	0.65 mm	0.75 mm	0.75 mm	0.20 mm	0.55 mm	0.60 mm
TwistResEq—HA	0.45 mm	0.70 mm	0.70 mm	0.15 mm	0.65 mm	0.70 mm
	9 Eq. it.	37 Eq. it.	117 Eq. it.	5 Eq. it.	20 Eq. it.	63 Eq. it.
TwistSensEq—LA	0.70 mm	0.75 mm	0.80 mm	0.15 mm	0.60 mm	0.65 mm
TwistSensEq—HA	0.45 mm	0.65 mm	0.70 mm	0.15 mm	0.60 mm	0.70 mm

CNR data

Table A3. Highest CNR values and their standard deviation obtained at low activity (12 MBq ml^{-1}) by the collimator designs tested for each sector.

	CNR ^{18}F			CNR ^{89}Zr		
d [mm]	CP	TwistResEq	TwistSensEq	CP	TwistResEq	TwistSensEq
0.60	0.20 ± 0.13	0.48 ± 0.05	0.44 ± 0.12	0.03 ± 0.14	0.08 ± 0.10	0.04 ± 0.20
0.65	0.64 ± 0.02	0.58 ± 0.08	0.69 ± 0.08	0.06 ± 0.20	0.15 ± 0.09	0.27 ± 0.10
0.70	1.74 ± 0.16	1.55 ± 0.07	2.10 ± 0.14	0.50 ± 0.08	0.37 ± 0.13	0.69 ± 0.02
0.75	2.28 ± 0.21	2.20 ± 0.06	2.45 ± 0.22	0.48 ± 0.13	0.59 ± 0.11	0.75 ± 0.36
0.80	3.13 ± 0.21	3.63 ± 0.20	3.17 ± 0.05	0.80 ± 0.17	1.17 ± 0.19	1.36 ± 0.20
0.90	4.04 ± 0.40	4.93 ± 0.45	4.54 ± 0.54	1.69 ± 0.16	2.33 ± 0.04	2.31 ± 0.28

Table A4. Highest CNR values and their standard deviation obtained at high activity (190 MBq ml^{-1}) by the collimator designs tested for each sector.

	CNR ^{18}F			CNR ^{89}Zr		
d [mm]	CP	TwistResEq	TwistSensEq	CP	TwistResEq	TwistSensEq
0.60	1.42 ± 0.13	1.24 ± 0.07	1.62 ± 0.09	0.17 ± 0.16	0.55 ± 0.09	0.76 ± 0.13
0.65	1.82 ± 0.04	1.91 ± 0.06	2.46 ± 0.16	0.41 ± 0.04	0.77 ± 0.09	1.21 ± 0.16
0.70	4.79 ± 0.53	3.88 ± 0.10	5.14 ± 0.31	1.68 ± 0.37	1.54 ± 0.11	2.31 ± 0.24
0.75	5.48 ± 0.11	5.15 ± 0.23	5.64 ± 0.35	2.26 ± 0.78	2.30 ± 0.32	3.34 ± 0.36
0.80	6.66 ± 0.44	7.28 ± 0.18	8.23 ± 0.23	3.43 ± 0.24	4.13 ± 0.32	4.58 ± 0.25
0.90	8.89 ± 0.60	8.62 ± 0.35	9.05 ± 0.23	5.39 ± 0.61	6.26 ± 0.25	6.78 ± 0.68

ORCID iDs

Valerio Cosmi https://orcid.org/0009-0008-2748-2202
Monika Kvassheim https://orcid.org/0000-0001-7985-1980
Satyajit Ghosh https://orcid.org/0000-0001-6334-1185
Marlies C Goorden https://orcid.org/0009-0007-2202-5371

References

Accorsi R and Metzler S D 2004 Analytic determination of the resolution-equivalent effective diameter of a pinhole collimator *IEEE Trans. Med. Imaging* **23** 750–63
Accorsi R and Metzler S D 2005 Resolution-effective diameters for asymmetric-knife-edge pinhole collimators *IEEE Trans. Med. Imaging* **24** 1637–46
Beekman F J 2011 *Focused pinhole gamma detection device US Patent* 8,067,741 B2

Beekman F J 2022 *A SPECT scanner and collimator US Patent* 0133246 A1
Beekman F J, Kamphuis C, Koustoulidou S, Ramakers R M and Goorden M C 2021 Positron range-free and multi-isotope tomography of positron emitters *Phys. Med. Biol.* **66** 065011
Bom V, Goorden M and Beekman F 2011 Comparison of pinhole collimator materials based on sensitivity equivalence *Phys. Med. Biol.* **56** 3199–214
Bruehlmeier M, Roelcke U, Bläuenstein P, Missimer J, Schubiger P A, Locher J T, Pellikka R and Ametamey S M 2003 Measurement of the extracellular space in brain tumors using 76Br-bromide and PET *J. Nucl. Med.* **44** 1210–8 (PMID: 12902409)
Conti M and Eriksson L 2016 Physics of pure and non-pure positron emitters for PET: a review and a discussion *EJNMMI Phys.* **3** 8
Cosmi V, Wang B, Goorden M C and Beekman F J 2024 NaI gamma camera performance for high energies: effects of crystal thickness, photomultiplier tube geometry and light guide thickness *Med. Phys.* **51** 4696–708
de Swart J, Chan H S, Goorden M C, Morgenstern A, Bruchertseifer F, Beekman F J, de Jong M and Konijnenberg M W 2016 Utilizing high-energy gamma-photons for high-resolution 213Bi SPECT in mice *J. Nucl. Med.* **57** 486–92
Goorden M C and Beekman F J 2010 High-resolution tomography of positron emitters with clustered pinhole SPECT *Phys. Med. Biol.* **55** 1265–77
Goorden M C, Kamphuis C, Ramakers R M and Beekman F J 2020 Accelerated image reconstruction by a combined dual-matrix dual-voxel approach *Phys. Med. Biol.* **65** 105014
Goorden M C, van der Have F, Kreuger R, Ramakers R M, Vastenhouw B, Burbach J P H, Booij J, Molthoff C F M and Beekman F J 2013 VECTor: a preclinical imaging system for simultaneous submillimeter SPECT and PET *J. Nucl. Med.* **54** 306–12
Goorden M C, van Roosmalen J, van der Have F and Beekman F J 2016 Optimizing modelling in iterative image reconstruction for preclinical pinhole PET *Phys. Med. Biol.* **61** 3712–33
Jan S *et al* 2004 GATE: a simulation toolkit for PET and SPECT *Phys. Med. Biol.* **49** 4543–61
Jauw Y W, Menke-van der Houven van Oordt C W, Hoekstra O S, Hendrikse N H, Vugts D J, Zijlstra J M, Huisman M C and van Dongen G A M S 2016 Immuno-positron emission tomography with zirconium-89-labeled monoclonal antibodies in oncology: what can we learn from initial clinical trials? *Front. Pharmacol.* **7** 131
Kuker R, Sztejnberg M and Gulec S 2017 I-124 imaging and dosimetry *Mol. Imaging Radionucl. Ther.* **26** 66–73
Laforest R and Liu X 2009 Cascade removal and microPET imaging with 76Br *Phys. Med. Biol.* **54** 1503–31
Lovqvist A, Sundin A, Roberto A, Ahlström H, Carlsson J and Lundqvist H 1997 Comparative PET imaging of experimental tumors with bromine-76-labeled antibodies, fluorine-18-fluorodeoxyglucose and carbon-11-methionine *J. Nucl. Med.* **38** 1029–35 (PMID: 9225786)
Mok G S P, Wang Y C and Tsui B M W 2009 Quantification of the multiplexing effects in multi-pinhole small animal SPECT: a simulation study *IEEE Trans. Nucl. Sci.* **56** 2636–43
Nguyen M P *et al* 2022 Ultra-high sensitivity simultaneous small animal PET-SPECT for microCi range imaging *J. Nucl. Med.* **63** 2344
Ogawa K, Harata Y, Ichihara T, Kubo A and Hashimoto S 1991 A practical method for position-dependent Compton-scatter correction in single photon emission CT *IEEE Trans. Med. Imaging* **10** 408–12
Vaissier P E, Beekman F J and Goorden M C 2016 Similarity-regulation of OS-EM for accelerated SPECT reconstruction *Phys. Med. Biol.* **61** 4300–15
Vaissier P E, Goorden M C, Vastenhouw B, van der Have F, Ramakers R M and Beekman F J 2012 Fast spiral SPECT with stationary gamma-cameras and focusing pinholes *J. Nucl. Med.* **53** 1292–9
van der Have F, Ivashchenko O, Goorden M C, Ramakers R M and Beekman F J 2016 High-resolution clustered pinhole (131)Iodine SPECT imaging in mice *Nucl. Med. Biol.* **43** 506–11
van der Have F, Vastenhouw B, Ramakers R M, Branderhorst W, Krah J O, Ji C, Staelens S G and Beekman F J 2009 U-SPECT-II: an ultra-high-resolution device for molecular small-animal imaging *J. Nucl. Med.* **50** 599–605
Vastenhouw B and Beekman F 2007 Submillimeter total-body murine imaging with U-SPECT-I *J. Nucl. Med.* **48** 487–93
Walker M D, Goorden M C, Dinelle K, Ramakers R M, Blinder S, Shirmohammad M, van der Have F, Beekman F J and Sossi V 2014 Performance assessment of a preclinical PET scanner with pinhole collimation by comparison to a coincidence-based small-animal PET scanner *J. Nucl. Med.* **55** 1368–74
Zhou Y, Baidoo K E and Brechbiel M W 2013 Mapping biological behaviors by application of longer-lived positron emitting radionuclides *Adv. Drug. Deliv. Rev.* **65** 1098–111